

MID-INFRARED DIAGNOSTICS OF THE CIRCUMNUCLEAR ENVIRONMENTS
OF THE YOUNGEST RADIO GALAXIESE. KOSMACZEWSKI¹, L. STAWARZ¹, A. SIEMIGINOWSKA², C. C. CHEUNG³, L. OSTORERO^{4, 5}, M. SOBOLEWSKA²,
D. KOZIEL-WIERZBOWSKA¹, A. WÓJTOWICZ¹, & V. MARCHENKO¹*Draft version May 17, 2022*

ABSTRACT

We present a systematic analysis of the mid-infrared (MIR) properties of the youngest radio galaxies, based on low-resolution data provided by the *WISE* and *IRAS* satellites. We restrict our analysis to sources with available X-ray data that constitute the earliest phase of radio galaxy evolution, i.e. those classified as Gigahertz Peaked Spectrum (GPS) and/or Compact Symmetric Objects (CSOs). In our sample of 29 objects, we find that the host galaxies are predominantly red/yellow ellipticals, with some of them displaying distorted morphology. We find a variety of MIR colors, and observe that the sources in which the MIR emission is dominated by the ISM component uniformly populate the region occupied by galaxies with a wide range of pronounced ($\geq 0.5 M_{\odot} \text{ yr}^{-1}$) star formation activity. We compare the MIR color distribution in our sample to that in the general population of local AGN, in the population of evolved FR II radio galaxies, and also in the population of radio galaxies with recurrent jet activity. We conclude that the triggering of radio jets in AGN does not differentiate between elliptical hosts with substantially different fractions of young stars; instead there is a relationship between the jet duty cycle and the ongoing star formation. The distribution of the sub-sample of our sources with $z < 0.4$ on the low-resolution MIR vs. absorption-corrected X-ray luminosity plane is consistent with the distribution of a sample of local AGN. Finally, we comment on the star formation rates of the two γ -ray detected sources in our sample, 1146+596 & 1718-649.

Subject headings: ISM: jets and outflows — galaxies: active — galaxies: jets — infrared: galaxies — X-rays: galaxies

1. INTRODUCTION

Compact radio sources constitute a particularly interesting, yet diverse, class of active galactic nuclei (AGN), with newly born radio structures (jets and lobes) fully confined within their host galaxies (see O’Dea 1998, for a review). As such, they provide direct insight into the mechanisms that lead to triggering the production of relativistic jets in AGN (e.g., Czerny & You 2016), as well as insight into the complex dynamics of feedback between evolving supermassive black holes and interstellar medium (e.g., Tadhunter 2016; Wagner et al. 2016).

To study these dynamics, specific evolutionary models for compact radio galaxies have been developed (e.g., Kawakatu et al. 2008), and certain predictions have been made regarding their multi-wavelength emission and absorption properties (e.g., Stawarz et al. 2008). These models have been tested against various multi-frequency datasets (Ostorero et al. 2010; Migliori et al. 2014). There, however, still remains a lack of consensus on the relative contribution from jets and lobes, accretion disks and circum-nuclear dusty tori, or, to some extent, the interstellar medium (ISM) itself, to the observed radia-

tive output of such systems at infrared, X-ray, and γ -ray photon energies.

In this context, we focus on a systematic investigation of the mid-infrared (MIR) properties of the most compact radio galaxies. These sources are confirmed spectroscopically in the radio domain as ‘GHz-peaked spectrum’ (GPS) sources, and/or morphologically (using high-resolution radio interferometers) as ‘compact symmetric objects’ (CSOs). In order to study the MIR properties, we utilize data provided by the Wide-field Infrared Survey Explorer (*WISE*), as well as archival data from the Infrared Astronomical Satellite (*IRAS*) augmented in a few cases by *Spitzer* Space Telescope observations. We restrict our sample only to those objects which have been observed in X-rays with either the *XMM-Newton* or the *Chandra* X-ray Observatory, so that multi-wavelength diagnostics can be applied to disclose the origins of the observed fluxes.

Previously, the infrared emission of GPS/CSOs had been analyzed by Heckman et al. (1994) in the mid-far infrared domain, based on low-resolution data from *IRAS*, and by Fanti et al. (2000) in the far infrared, using the Infrared Space Observatory (ISO) data. These authors argued that the mid-to-far infrared emission of compact radio galaxies is comparable to that of the extended radio galaxies with matching radio powers and redshifts. Therefore, these sources are most likely dominated by an AGN component, the hot dusty tori in particular.

emily@oa.uj.edu.pl

¹ Astronomical Observatory of the Jagiellonian University, ul. Orla 171, 30-244 Kraków, Poland² Center for Astrophysics, Harvard & Smithsonian, 60 Garden Street, Cambridge, MA 02138, USA³ Naval Research Laboratory, Space Science Division, Code 7650, Washington, DC 20375, USA⁴ Dipartimento di Fisica, Università degli Studi di Torino, Via P. Giuria 1, I-10125 Torino, Italy⁵ Istituto Nazionale di Fisica Nucleare (INFN), Sezione di Torino, Via P. Giuria 1, I-10125 Torino, Italy

TABLE 1
MIR PROPERTIES OF X-RAY DETECTED CSOS

Name	z	d_L [Mpc]	LS [pc]	class	W1–W2 [mag]	W2–W3 [mag]	WISE color	IRAS $L_{12\mu m}$ [10^{43} erg/s]	MIPS $L_{24\mu m}$ [10^{43} erg/s]	WISE $L_{12\mu m}$ [10^{43} erg/s]	$L_{2-10\text{ keV}}$ [10^{43} erg/s]	Ref.
(1)	(2)	(3)	(4)	(5)	(6)	(7)	(8)	(9)	(10)	(11)	(12)	(13)
0019-000	0.305	1521	220	GPS	0.472	2.441	S	–	–	3.53 \pm 0.11	0.55 [^]	T09
0026+346	0.517	2852	190	GPS	0.743	2.491	Un	–	–	21 \pm 0.3	23 \pm 2	G06
0035+227	0.096	418	21.8	CSO	0.148	1.265	E	–	–	0.425 \pm 0.007	0.075 \pm 0.034	S16
0108+388	0.669	3907	22.7	CSO	0.132	3.159	S	9.86 \pm 9.16	3.79 \pm 1.40	<13.1	7 \pm 3	T09,S16
0116+319	0.059	255	70.1	CSO	0.035	1.682	S*	0.595 \pm 0.056	0.609 \pm 0.046	0.629 \pm 0.003	<0.10 [†]	S16
0402+379	0.055	234	7.3	CSO	0.099	1.721	S	0.48 \pm 0.07	0.949 \pm 0.059	0.608 \pm 0.004	0.041 \pm 0.016	R14
0428+205	0.219	1044	653	GPS	0.323	2.648	S	–	–	3.93 \pm 0.08	1.4 \pm 0.6	T09
0500+019	0.585	3319	55	GPS	0.585	2.892	Q	63.4 \pm 6.5	87.2 \pm 9.8	59.3 \pm 0.5	50 \pm 6	T09
0710+439	0.518	2868	87.7	CSO	0.726	2.997	Sy	43.8 \pm 4.4	107 \pm 7	43.4 \pm 0.4	39.40 \pm 3.15	T09,S16
0941-080	0.228	1100	148	GPS	0.388	2.444	S	–	–	2.57 \pm 0.05	0.091 \pm 0.075	T09
1031+567	0.460	2480	109	CSO	0.999	2.922	Q	17.6 \pm 3.0	16.5 \pm 4.7	15.6 \pm 0.3	2.2 \pm 0.2	T09,S16
1117+146	0.362	1874	306	GPS	0.406	3.599	SB	–	–	<5.87	1.40 \pm 0.19	T09
1146+596	0.011	47	933 [◊]	CSO [•]	–0.011	1.237	E	0.0816 \pm 0.0022	0.0818 \pm 0.0033	0.1010 \pm 0.0002	0.007	U05
1245+676	0.107	478	9.6	CSO	0.130	1.409	E	0.33 \pm 0.14	0.358 \pm 0.098	0.531 \pm 0.006	0.031 ^{††}	W09,S16
1323+321	0.368	1908	247	GPS	0.303	2.014	S	–	–	2.54 \pm 0.11	3.7 \pm 0.4	T09
1345+125	0.122	551	166	CSO	1.308	3.930	Sy*	83.3 \pm 1.7	216 \pm 4	87.9 \pm 0.2	7.8 \pm 1.5	T09,J13
1358+624	0.431	2298	218	GPS	1.210	2.592	Q*	31.0 \pm 2.4	37.8 \pm 2.8	35.4 \pm 0.2	30 \pm 20	T09
1404+286	0.077	336	10.0	CSO	1.018	3.063	Q	50.9 \pm 0.9	65.2 \pm 1.3	51.6 \pm 0.1	0.45 \pm 0.06 ^C	T09,S16,S19b
1511+0518	0.084	370	7.3	CSO	1.233	2.899	Q	–	51.1 \pm 3	52.2 \pm 0.1	3 ^C	S16
1607+268	0.473	2569	240	CSO	0.287	2.679	S*	4.21 \pm 3.17	21.6 \pm 4.4	<7.27	3.79 \pm 0.87	T09,S16
1718-649	0.014	60.4	2.0	CSO	0.136	2.462	S	0.322 \pm 0.009	0.32 \pm 0.01	0.401 \pm 0.001	0.0154 \pm 0.0024	S16
1843+356	0.763	4612	22.3	CSO	1.160	4.047	Sy	–	–	190 \pm 1	5.60 \pm 2.28	S16
1934-638	0.183	845	85.1	CSO	0.609	3.360	Sy	5.89 \pm 0.62	19 \pm 1	6.52 \pm 0.03	0.60 \pm 0.14	S16,S19a
1943+546	0.263	1285	107.1	CSO	0.628	2.191	Un	–	–	5.64 \pm 0.04	0.73 \pm 0.28	S16
1946+708	0.101	444	39.4	CSO	0.663	2.336	Un	1.75 \pm 0.15	1.67 \pm 0.10	1.69 \pm 0.01	1.20 \pm 0.18	S16,S19a
2008-068	0.547	3056	218	CSO	0.334	2.159	S	–	7.68 \pm 0.35	9.1 \pm 0.4	6 \pm 2	T09
2021+614	0.227	1086	16.1	CSO	1.287	3.009	Q	<210	–	64.9 \pm 0.2	11.2 ^C	S16,S19a
2128+048	0.990	6364	218	GPS	0.688	3.352	Sy	–	63.9 \pm 2.3	<52.4	29 \pm 4	T09
2352+495	0.238	1143	117.3	CSO	0.688	2.714	Sy	–	–	4.25 \pm 0.04	1.3 \pm 0.3	T09,S16

col(1) — name of the source; **col(2)** — redshift; **col(3)** — luminosity distance; **col(4)** — linear size of the radio lobes taken from the references provided in col(13), [◊] except of 1146+596 cited from [Perlman et al. \(2001\)](#); **col(5)** — morphological/spectral radio classification: Compact Symmetric Object (CSO) based on the morphology, Gigahertz Peaked Spectrum (GPS) based on the spectral classification; classification follows the references given in col(13), [•] except of 1146+596 following from [Perlman et al. \(2001\)](#); **col(6)** — *WISE* Difference in the W1 (3.4 μm) and W2 (4.6 μm) color bands; **col(7)** — *WISE* Difference in the W2 (4.6 μm) and W3 (12 μm) color bands; **col(8)** — color classification: “Elliptical” (E), “Spiral” (S), “Starburst” (SB), Quasar/Seyfert (Q/Sy), “Uncertain” (Un); possible contamination of *WISE* fluxes by background/foreground sources denoted by *; **col(9)** — *IRAS* 12 μm luminosity; **col(10)** — *Spitzer*/MIPS 24 μm luminosity; **col(11)** — *WISE* 12 μm luminosity calculated from the W3 band magnitude; **col(12)** — unabsorbed 2–10 keV luminosity taken from the references provided in col(13); [^] extrapolated from the detection in the 0.5–2 keV band with photon index = 1.61; [†] estimated from the 0.5–2.0 keV upper limit $< 0.5 \times 10^{-14}$ erg cm⁻² s⁻¹ assuming photon index = 2.0; ^{††} calculated based on the 4.5–12.0 keV PN flux; ^C value corresponding to the “Compton-thick” scenario; **col(13)** — X-ray references: [Guainazzi et al. \(2006\)](#) [G06], [Jia et al. \(2013\)](#) [J13], [Romani et al. \(2014\)](#) [R14], [Siemiginowska et al. \(2016\)](#) [S16], [Sobolewska et al. \(2019a\)](#) [S19a], [Sobolewska et al. \(2019b\)](#) [S19b], [Tengstrand et al. \(2009\)](#) [T09], [Ueda et al. \(2005\)](#) [U05], [Watson et al. \(2009\)](#) [W09].

More recently, Willett et al. (2010) presented the MIR observations of eight nearby CSOs (redshifts $z \lesssim 0.1$) from *Spitzer*, finding a diversity in their spectral properties. An overwhelming majority of the sources in their sample displayed a contribution from both circumnuclear dust, heated by the central AGN, and star formation activity within the host galaxy. Willett et al. (2010) argued, moreover, that the star formation rates in the studied sources, estimated at the level of $(0.3 - 50) M_{\odot} \text{ yr}^{-1}$ based on the detected polycyclic aromatic hydrocarbon (PAH) emission, implies a close link between the triggering of radio jets and galaxy mergers. On the other hand, Tadhunter et al. (2011) and Dicken et al. (2012) proposed that the enhanced star formation activity in compact radio sources over that observed in evolved radio galaxies, indeed seen in their flux limited samples, may be instead due to an observational selection effect. This follows from the enhanced radiative efficiency of compact radio-emitting jets and lobes in the former class of objects (see also O’Dea 2016, for the discussion).

In the X-ray domain, the first dedicated studies of GPS/CSOs with the high-angular resolution telescopes XMM-Newton and Chandra, have been reported by Guainazzi et al. (2004, 2006); Vink et al. (2006); Siemiginowska et al. (2008, 2009, 2016); Tengstrand et al. (2009), and Sobolewska et al. (2019a,b). Since the radio structures of the targeted sources remain unresolved even on arcsec scales, various origins of the detected fluxes within the 0.1–10 keV range have been considered by these authors including: accretion disk coronal emission, jet/lobe non-thermal radiation, as well as emission of hot gas within the ISM, modified (shocked) by expanding compact radio structures.

In most cases, unfortunately, rather limited photon statistics preclude any more in-depth spectral modeling, which would enable a robust discrimination between various emission models. The X-ray continua of compact radio galaxies were typically found to be consistent with a single power-law, with photon indices $\Gamma \sim 1 - 2$, moderated by hydrogen column densities $N_{\text{H}} \lesssim 10^{22} \text{ cm}^{-2}$. Such spectra could be accommodated by either the disk coronal emission scenario, with modest intrinsic absorption, or the model in which observed X-ray fluxes are dominated by inverse-Comptonization of various ambient photon fields (and the infrared emission of circumnuclear dusty tori in particular) within compact radio lobes shining through the ISM of host galaxies (Ostorero et al. 2010). Only in a few cases, subjected to deeper exposures (1404+286, 1511+0518 and 2021+614), was there a detection of the neutral fluorescence iron line and/or hydrogen column densities in excess of 10^{23} cm^{-2} , indicating the disk coronal emission is seen through a Compton-thick circumnuclear tori (Guainazzi et al. 2004; Siemiginowska et al. 2016; Sobolewska et al. 2019a,b). On the other hand, for the particular case of 1718–649, the observed X-ray emission appeared contributed to by a hot, collisionally ionized gas located within the central parts of the host galaxy (Siemiginowska et al. 2016; Beuchert et al. 2018).

Below, in Section 2 we discuss the selection of the sample including the most compact radio galaxies observed in X-rays. In Section 3 we describe the MIR

data acquisition for the selected sources, specifically the *WISE*, *IRAS*, and *Spitzer* archival observations. In Section 4 we discuss the results of our analysis, and our main conclusions are outlined in Section 5. Throughout the paper we assume modern Λ CDM cosmology with $H_0 = 70 \text{ km s}^{-1} \text{ Mpc}^{-1}$, $\Omega_{\text{m}} = 0.3$, and $\Omega_{\Lambda} = 0.7$.

2. SAMPLE SELECTION

As mentioned in Section 1 above, in this paper we consider only radio galaxies (i) for which the redshifts are measured, (ii) are characterized by compact radio structures with linear sizes $LS < 1 \text{ kpc}$, and are classified morphologically as CSOs and/or spectrally as GPS sources, and (iii) that have available X-ray data. After a careful inspection of literature studies, we construct a “master sample” of such objects, the majority of which make up the samples discussed by Tengstrand et al. (2009) and Siemiginowska et al. (2016), with the addition of 0026+346, 0402+379, and 1146+596 (see Guainazzi et al. 2006; Willett et al. 2010; Ostorero et al. 2017). This amounts to a total of 29 targets, including 27 that have been detected in X-rays by either XMM-Newton or Chandra, one source with the X-ray flux measured by ASCA (1146+596; see Ueda et al. 2005)⁶, and one source having a Chandra upper limit for its 0.5 – 2.0 keV flux (0116+319; see Siemiginowska et al. 2016). Table 1 summarizes the basic information for the given sample, in particular, the 2 – 10 keV and MIR luminosities.

In the accompanying paper by Wójtowicz et al. (2019), we considered a smaller sample of the youngest X-ray detected radio galaxies, by imposing a much more restrictive selection criteria, namely (i) measured redshifts, (ii) strictly CSO morphological classification, in addition with *measured kinematic ages*, (iii) core X-ray fluxes measured with either XMM-Newton or Chandra. All of the 17 sources analyzed by Wójtowicz et al. are included in our master sample as well.

On the other hand, in our master sample we do not include X-ray detected compact radio galaxies lacking any robust GPS or CSO classification (e.g., 0046+316, 1146+531, 1217+295, 1231+481, 1254+571; see Sobolewska et al. 2019a), or classified before as GPS/CSOs but more recently re-classified as blazars (e.g., 1413+135; see Willett et al. 2010). We also do not discuss here the more evolved radio galaxies, classified morphologically as Medium Symmetric Objects (MSOs), and/or spectrally as Compact Steep Spectrum (CSS) sources (see Kunert-Bajraszewska et al. 2014). Finally, we do not include the Fanaroff-Riley type 0 (FR0) radio galaxies (Glowacki et al. 2017; Torresi et al. 2018).

3. MIR DATA ACQUISITION

3.1. MIR Data

In this study we utilize three infrared telescopes: the Wide-field Infrared Survey Explorer (*WISE*), the Infrared Astronomical Satellite (*IRAS*), and the *Spitzer* instrument, the Multiband Imaging Photometer (*MIPS*) for NASA’s Space Infrared Telescope Facility (*SIRTF*). Each instrument has differing operating capabilities, all of which are detailed below.

⁶ The analysis of the archival and previously unpublished *Chandra* data for 1146+596 will be presented in a forthcoming paper.

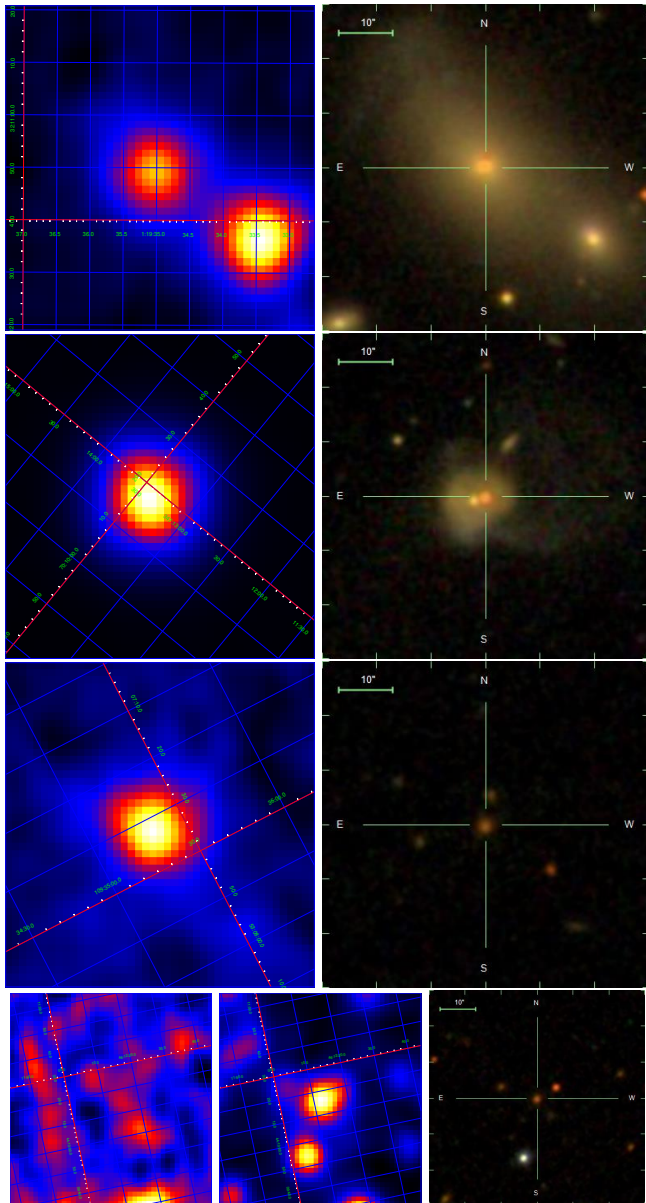


FIG. 1.— *WISE* 12 μm images with overlaid ecliptic coordinate grids (left panels), along with the SDSS gri color composite images (right panels) for 0116+319, 1345+125, 1358+642, and 1607+268 (rows from top to bottom). In the case of 1607+268 (bottom row), the *WISE* 3.4 μm image is presented in addition (central panel). Images are equal in size, being a square 60''.

WISE is an all sky survey mission covering the entirety of the northern and southern sky. The telescope obtains measurements in four bands (W1–W4) centered at 3.4, 4.6, 12, and 22 μm respectively. The resolution in each of the bands is as follows: 6.1'', 6.4'', 6.5'', & 12'' in each of the four bands (W1, W2, W3, W4; Wright et al. 2010).

IRAS surveys the sky at slightly longer wavelengths than *WISE*; its bands are centered at 12, 25, 60 and 100 μm . We utilize the 12 μm measurements for this work with a resolution of 0.5', notably larger than *WISE*. It is prudent to note that the *IRAS* 12 μm band has a width of 6.5 μm , whereas the *WISE* 12 μm has a band width of 5.5 μm . This results in the *IRAS* measurements being on average slightly higher than the *WISE* measurements.

MIPS images the sky with bands centered at: 24, 70, and 160 μm . For this work we inspect the 24 μm measurements with a given resolution of 6'', comparable to *WISE*.

3.2. Source Contamination

Due to the angular resolution of *WISE*, and the significantly lower resolution of the *IRAS* instrument, source contamination due to galaxies in close proximity to our sources is possible. In order to diagnose any potential contamination, visual inspection of optical and infrared images of all sources in our sample was performed to assess if any contaminating objects lie within the field of view of the *WISE* or *IRAS* instruments. This inspection was paired with a literary search using the NASA/IPAC Extragalactic Database (NED) to identify the classification of any objects within 12'' of our sources. For this search, we restrict our inspection to only galaxies and stellar objects as their infrared luminosities are significant enough to cause a detectable shift in the infrared measurements of our sources. We note that we do not consider any unresolved infrared sources as contaminating objects.

We conclude that contamination in the *WISE* bands is possible in 8 of the 29 sources in our sample. Out of these, the following sources are expected to only have contamination in the longest-wavelength *WISE* band, W4 (resolution of 12''), which we do not use for our color classification or in further analysis: 0019 – 000, 1031+567, 1117+146 and 1323+321. Therefore, for these four sources, the *WISE* color classification is expected to be unaffected by the nearby galaxies/stars, however, there is a potential for mild contamination in their *IRAS* fluxes. We note that from these only 1031 + 567 has available *IRAS* flux measurements, and the difference in the measured flux between the *IRAS* and *WISE* is 12%, see Table 1.

Contamination in the *WISE* color classification for the following sources is likely: 0116 + 319, 1345 + 125, 1358 + 624, and 1607 + 268, all marked in Table 1. These sources have galaxies and/or stars closer than 6.5'', and as such would contain some level of excess flux in all four *WISE* bands and result in a shift in the positioning on our diagnostic plot. These four cases can be viewed in Figure 1, which displays the *WISE* 12 μm image and the respective Sloan Digital Sky Survey (SDSS) color composite image of each source. Optical images are color composite images of the g(4770 Å), r(6231 Å), and i(7625 Å) bands obtained through the SDSS sky server. It can be clearly seen that the *WISE* images show a blending or merging of nearby objects that in the SDSS image are more clearly seen as separate objects. For the specific case of 1607+268 which has a very low flux in the 12 μm band; we provide the 3.4 μm band image as well.

We finally note one source in particular, 2021 + 614, which shows a significant difference between the *IRAS* and *WISE* flux measurements. The calculated *IRAS* luminosity is 223% higher than the respective *WISE* luminosity. This is most likely due to unresolved infrared sources near to 2021 + 614 as well as poor data quality provided by *IRAS*. We comment, however, that the difference in the fluxes provides little change to our conclusions.

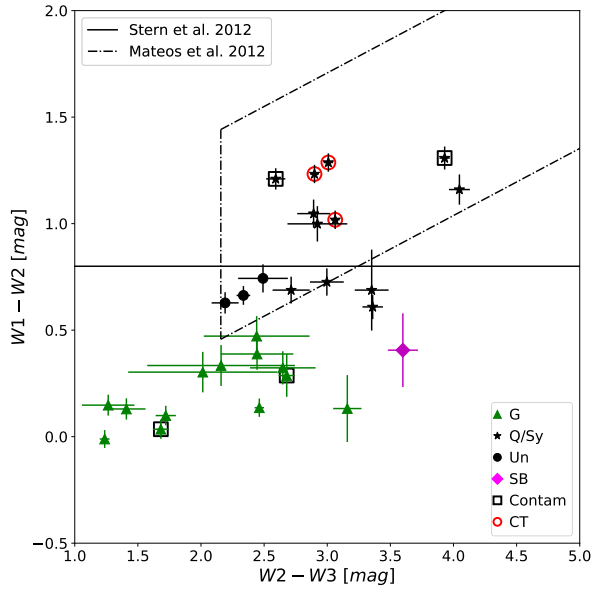


FIG. 2.— *WISE* color-color diagram for compact radio galaxies included in our sample. Different symbols denote *WISE* color classification following Wright et al. (2010): “Galaxy” (G) – green triangle, “Starburst” (SB) – purple side-pointing triangle, “Quasar/Seyfert” (Q/Sy) – black star, “Uncertain” (Un) – black circle; sources marked with a black square may have a significant contamination from nearby background/foreground objects; red circles indicate objects confirmed as Compton-thick based on the X-ray spectroscopy. The horizontal solid line delineates the Stern et al. (2012) cut: the MIR emission of sources located above the line is dominated by an AGN component. The dotted, dashed lines show the Mateos et al. (2012) cut: the MIR emission of sources located within wedge is dominated by an AGN component.

3.3. MIR Photometry

The *WISE* colors, $W1-W2$ and $W2-W3$, can be utilized to diagnose the suggested level of star formation within a source and suggest the type of source being observed. The *WISE* colors for all sources in our sample have been estimated in a standard manner based on photometry in the $W1$ ($3.4\,\mu\text{m}$), $W2$ ($4.6\,\mu\text{m}$), and $W3$ ($12\,\mu\text{m}$) bands. The $W1-W2$ and $W2-W3$ color values are provided in Table 1, and plotted in Figure 2. Based on those colors, and following the diagnostic plot provided in Wright et al. (2010), we have grouped our sources into distinct types denoted as “Elliptical” (E), “Spiral” (S), “Starburst” (SB), Quasar/Seyfert (Q/Sy), or — if the color falls in a non-defined region of the diagnostic plot — “Uncertain” (Un).

Infrared magnitudes were obtained for all 29 sources from *WISE*, and their luminosities were calculated using standard flux relations. In addition, $12\,\mu\text{m}$ were obtained from *IRAS* measurements for 16 out of the 29 sources, with the corresponding luminosities provided in Table 1. We provide the $12\,\mu\text{m}$ *IRAS* and $24\,\mu\text{m}$ *MIPS* luminosities for comparison with the obtained *WISE* values. We note that all but four sources have comparable $24\,\mu\text{m}$ *MIPS* luminosities to the $12\,\mu\text{m}$ *WISE* and *IRAS* measurements. 0710+439, 1345+125, 1607+268, and 1934-638 show an increase of 140–210% in the $24\,\mu\text{m}$ band, are all classified as Sy, and are all morphologically classified

as CSO. We note these four sources for further investigation in a follow-up paper, as potentially interesting sources to inspect spectroscopically.

An archival search was performed utilizing the *Spitzer* Heritage Archive which yielded mid infrared spectroscopic data for 15 out of 29 sources. The high-resolution *Spitzer* spectra is also available for several objects in the sample (see Willett et al. 2010; Ostorero et al. 2010). The spectra for these objects will be analyzed/re-analyzed and discussed in the follow-up paper.

4. RESULTS & DISCUSSION

4.1. *WISE* Colors and Host Galaxy Morphologies

Figure 2 presents the *WISE* color diagnostic plot, with different symbols reflecting the *WISE* color identification following Wright et al. (2010). Clearly, such an identification does not serve as a rigorous classification, as it only points out the most likely origin of the detected MIR fluxes, corresponding to either the ISM with various levels of the star formation activity (E, S, SB) or the AGN component (Q/Sy).⁷ Quasar and Seyfert like galaxies are collected into one group due to significant overlap of their individual regions in the color-color diagram, however, we differentiate these sources in Table 1. This identification is, on the other hand, consistent with the selection cut introduced by Stern et al. (2012), and represented in the figure by a solid horizontal line: all the young radio galaxies with the *WISE* colors of the Q/Sy type, are indeed located either very close to the line, or much above it, and this substantiates the dominant AGN (dusty torus) contribution to the MIR emission in their cases. The overwhelming majority of our sources with the *WISE* classifications of Q/Sy, as well as all classified as Uncertain, fall within the Mateos et al. (2012) cut, which constitutes a reliable MIR color selection of luminous AGN, constructed based on the flux-limited wide-angle Bright Ultrahard XMM-Newton Survey (BUXS; $4.5 - 10\,\text{keV}$ flux limit of $6 \times 10^{-14}\,\text{erg s}^{-1}\,\text{cm}^{-2}$).

Let us comment here on a few cases from our sample with “uncertain” *WISE* color identification. These sources lie, in fact, within the so-called “blazar strip” (Massaro et al. 2012), which may suggest that their MIR fluxes are dominated by a non-thermal jet-related emission. Unlike in blazar sources, however, such an emission does not have to be relativistically beamed, but instead may constitute a high-energy tail of the synchrotron continuum of compact radio lobes expanding with sub-relativistic ($\lesssim 0.1c$) velocities (see in this context the broad-band modelling by Ostorero et al. 2010).

Interestingly enough, all the objects in the sample confirmed as Compton-thick, based on the X-ray spectroscopy (1404+286, 1511+0518 and 2021+614; see Siemiginowska et al. 2016; Sobolewska et al. 2019a,b, respectively), are characterized by the *WISE* colors as being consistent with a quasar identification, as in fact expected. Hence, *WISE* color diagnostics could, in general, be considered as a very useful tool when selecting candidates for Compton-thick AGN among compact radio galaxies.

⁷ Note in this context the overlaps between different types of galaxies in the *WISE* color classification: for example 1345+125, denoted here as “Sy”, can additionally be classified as Ultraluminous Infrared Galaxy (ULIRG; e.g., Rodríguez Zaurín et al. 2009).

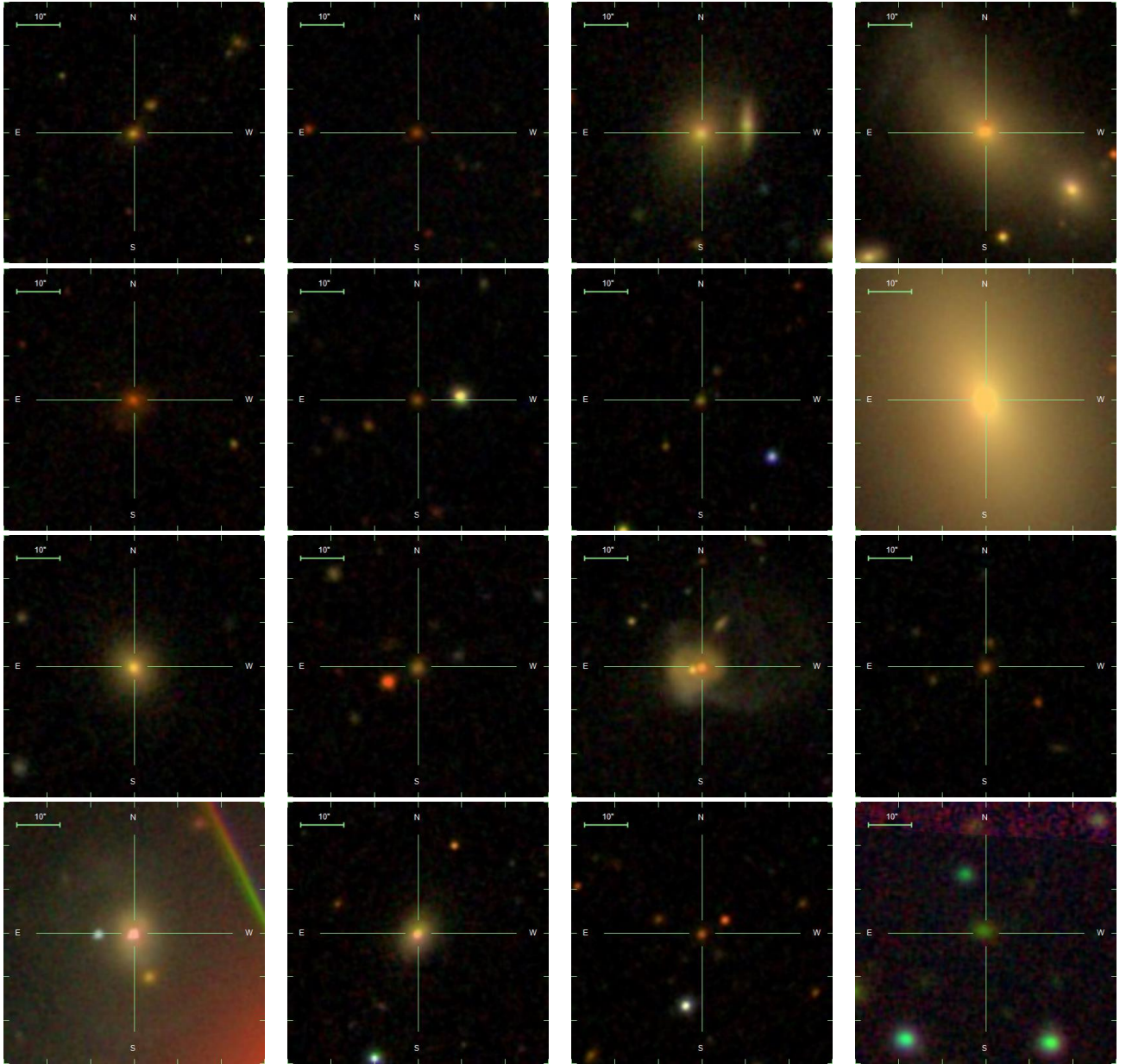


FIG. 3.— The SDSS gri color composite images of the host galaxies, available for 17 sources from our list (Abolfathi et al. 2018), excluding the particularly faint 2128+048; these are (from left to right) 0019–000, 0026+346, 0035+227, 0116+319 (first row), 0428+205, 1031+567, 1117+146, 1146+596 (second row), 1245+676, 1323+321, 1345+125, 1358+624 (third row), 1404+28, 1511+0518, 1607+268, 2352+495 (fourth row). In each image, the position of the source is indicated by a cross, while the image scale is shown in the upper left corner, with each image being a square $60''$.

The most striking feature of the diagram is, however, the fact that the most compact radio galaxies with colors $W1-W2 \leq 0.5$ mag, i.e. those presumably dominated in MIR by the ISM radiative output, populate almost uniformly the entire region occupied by galaxies (from elliptical to starbursts) with the $W2-W3$ colors between 1.0 and 4.0, suggesting a wide range of pronounced star formation activity within their hosts. Such a diversity could imply that the triggering of radio jets in AGN is not differentiated between hosts with substantially different fractions of young stars.

In this context, we investigate the optical images of the host galaxies in our sample. SDSS images of the host galaxies (Abolfathi et al. 2018) are available for 17

sources from our list; these are shown in Figure 3 (excluding the particularly faint 2128+048). In each image, the position of the source is indicated by a cross, while the image scale is shown in the upper left corner. These images are combined color images of the u, g, r, i, and z optical bands, obtained through the SDSS DR15 Navigate Tool. The SDSS images of the majority of our galaxies allow for an approximate morphological classification (the only exceptions are 2128+048, which is too faint to be classified, and 2352+495, whose image shows false colors). Most of the sources are red/yellow galaxies with an elliptical shape. Five galaxies have distorted morphology or show the signs of galaxy interaction; these are 0035+227, 0116+319, 0428+205,

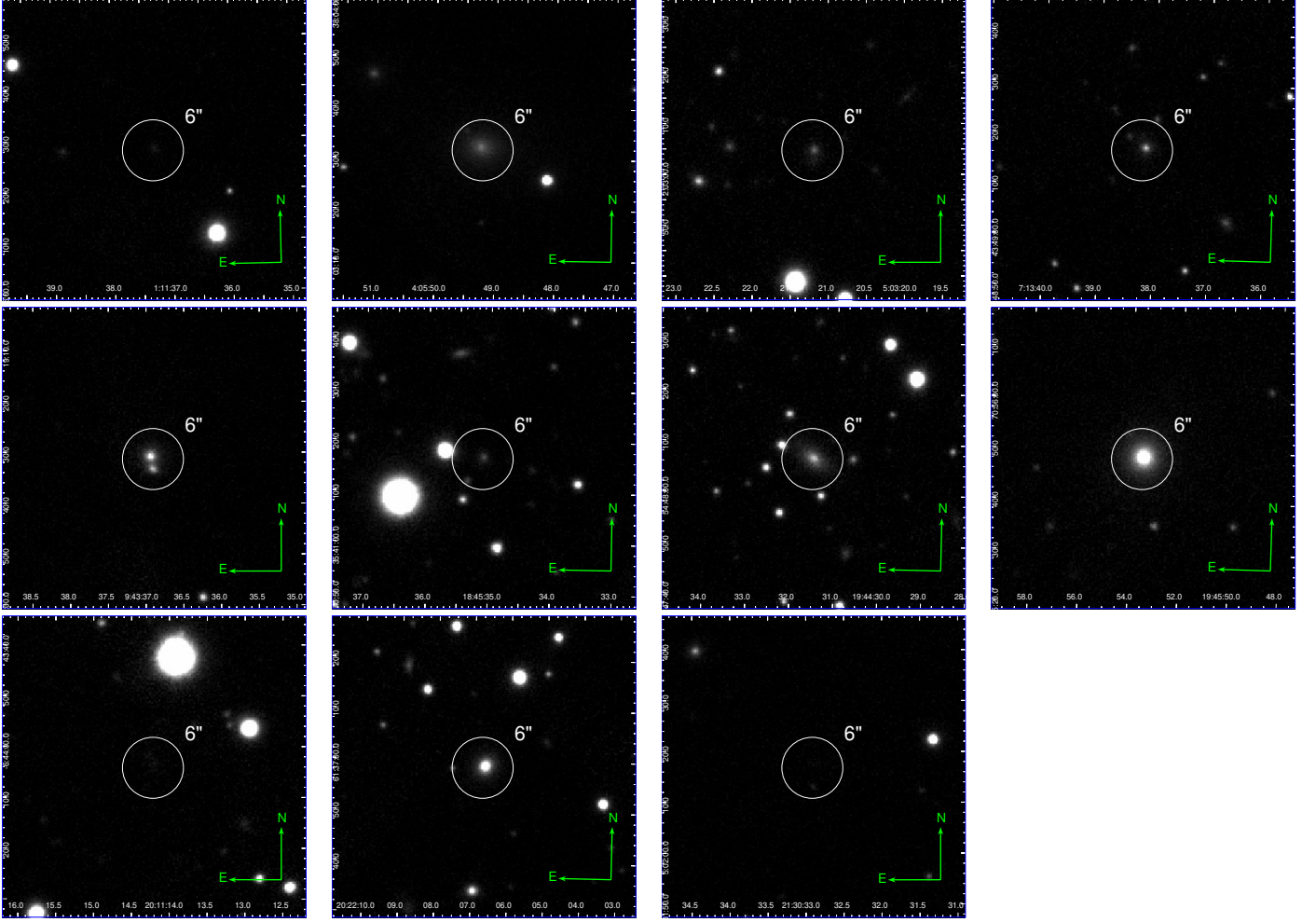


FIG. 4.— Optical images of sources not covered by SDSS (or too faint for SDSS), but observed instead by the all sky survey PanSTARRS, in the i band (7563 Å), including (from left to right) 0108+388, 0402+379, 0500+019, 0710+439 (first row), 0941–080, 1843+356, 1943+546, 1946+708 (second row), 2008–068, 2021+614, and 2128+048 (third row). In each image with overlaid ecliptic coordinate grids, the position of the source is indicated by a circle with a diameter of 6'' with each image being a square 60''.

1345+125, and 1404+286. None of the galaxies classified as spirals in the MIR color diagram shows the indication of a spiral structure. On this basis, we can conclude that the MIR colors differentiate galaxies with different levels of star formation, but they are loosely related to morphological types.

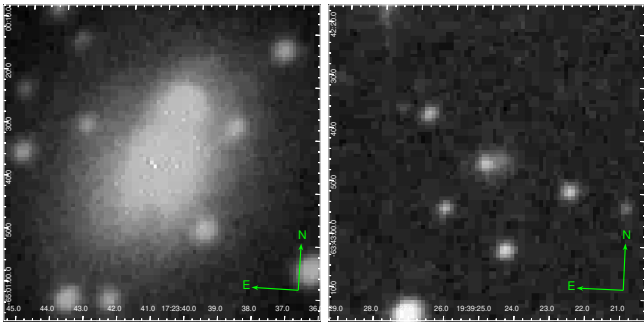


FIG. 5.— Additional optical images in the UKST blue band of the two southernmost sources 1718–649 (left panel) and 1934–638 (right panel), obtained from the Super Cosmos Sky Surveys. In each image, the position of the source is in the center of the image with each image being a square 60'' and containing overlaid ecliptic coordinate grids.

For the remaining sources which are not covered by the SDSS, or which are too faint for the SDSS, we retrieved the optical images of the hosts from the all sky survey PanSTARRS, in the i band (7563 Å), and, in the case of the two southernmost objects 1718–649 and 1934–638, from the Super Cosmos Sky Surveys in the UKST blue band; these are shown in Figures 4 and 5, respectively. Again, most of those galaxies whenever bright enough to be classified morphologically, display elliptical shapes, with the exception of the peculiar 1718–649 host, “*having the appearance of a high luminosity elliptical with faint outer spiral structure*” as noted by [Fanti et al. \(2000\)](#). We comment more on this object in Section 4.3. These images are shown as strictly optical intensity and as such no comments on their colors are made. We note that 0108+388, 2008–068, and 2128+048 are too faint in optical for any classification.

It is interesting to compare the distribution of the *WISE* colors in our sample of young radio galaxies with comparison samples of various types of active galaxies. For this purpose, we consider first the list of local (redshifts $z < 0.4$) AGN compiled by [Asmus et al. \(2014\)](#), which includes 102 sources selected from the nine

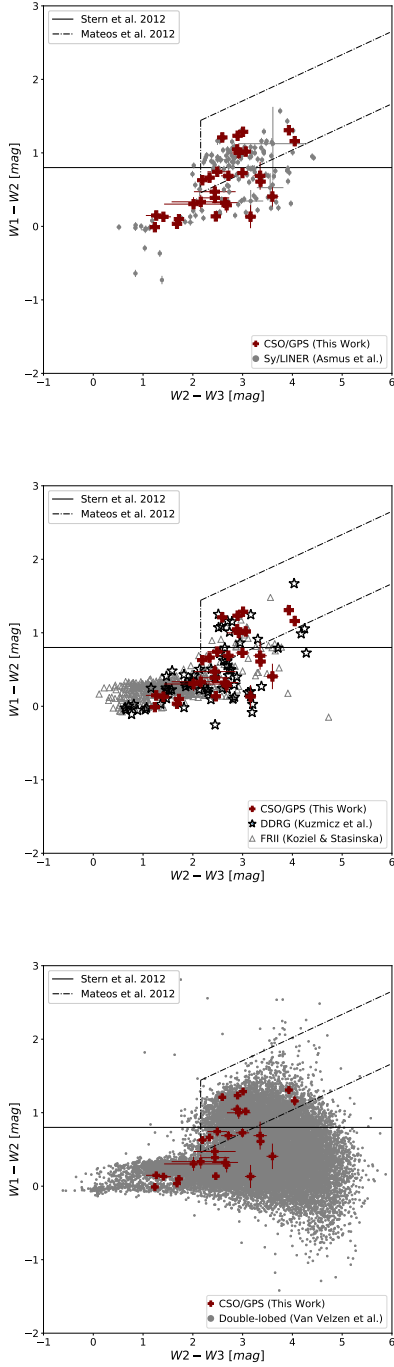


FIG. 6.— Top panel: A comparison of the Asmus et al. (2014) AGN sample of local Seyferts and LINERs with our sample of 29 GPS/CSO sources. Small grey symbols denote the AGN from the Asmus et al. sample. Middle panel: A comparison of the Kuźmicz et al. (2017) sample of restarted radio galaxies (DDRGs), along with the Kozieł-Wierzbowska, & Stasińska (2011) sample of the evolved classical doubles (FR II-type radio galaxies), with our sample of 29 GPS/CSO sources. Empty grey triangles denote FR IIs and filled blue circles denote DDRGs. Bottom panel: A comparison of the Van Velzen et al. (2015) double-lobed radio sources sample with our sample of 29 GPS/CSO sources. Small grey symbols denote the FR IIs from the Van Velzen et al. sample. The displayed cuts in all panels are the same as in Figure 2. Larger red crosses in each panel indicate the objects in our sample.

months of observations with the Burst Alert Telescope (BAT) onboard the *Swift* satellite within the 14–195 keV band (constituting a flux limited sub-sample in the list), complemented by the AGN with the available high-resolution MIR imaging enabled by ground-based 8m class telescopes such as VLT/VISIR, Gemini/Michelle, Subaru/COMICS, or Gemini South/T-ReCS. All together there are 253 sources in the Asmus et al. sample, for which the optical spectroscopic classification includes Seyferts type I, Seyferts type II, LINERs, and AGN/starburst composites. Moreover, the AGN from this sample are hosted by various types of galaxies, including late type galaxies with bona-fide spiral structures, not only elliptical or disk systems.

The distribution of the *WISE* colors for the Asmus et al. (2014) sample, in a direct comparison with our sample of GPS/CSOs, is shown in the top panel of Figure 6. Both distributions appear very similar and we quantify this statement by performing the two-dimensional Kolmogorov-Smirnov (2D KS) test, that was developed through the efforts to generalize the classical one-dimensional KS test to two (Peacock 1983) and higher dimensions (Fasano, & Franceschini 1987). In particular, we follow the 2D KS algorithm described in Fasano, & Franceschini (1987) and calculate — under the null hypothesis that the two analyzed samples were drawn from the same distribution — the two-tailed p -value (i.e., the probability of obtaining a value of the statistic D greater than the observed value, if the null-hypothesis were true). As a result, we obtain $p = 0.048$ and $D = 0.3$; adopting a significance level of $\alpha = 0.05$, this result implies that the null hypothesis has to be rejected. However, we note that a value of $p = 0.048$ is close to the rejection threshold.

We note that the Asmus et al. (2014) sample includes both radio-quiet and also radio-loud objects — either low-power radio galaxies of the Fanaroff-Riley type I (FR Is), or high-power classical doubles, i.e. Fanaroff-Riley type II radio galaxies (FR IIs) — however, the radio properties were not taken into account when selecting the sample. That is, neither a detection of a radio counterpart nor a particular threshold value for the radio loudness parameter constituted a selection criterion. It is therefore interesting that the distribution of the *WISE* colors for this “hard X-ray selected/quasi MIR selected” sample of local AGN with the median redshift $z = 0.016$, is statistically similar (even with the null hypothesis being rejected) to the distribution of *WISE* colors in our sample of the youngest radio galaxies, selected based on their radio properties and availability of X-ray data, and in addition spanning a wider range of redshifts from 0.011 up to 0.99, with the median of $z = 0.238$.

Second, we compare the MIR colors of our GPS/CSOs with those characterizing the *evolved* (extended) FR II type radio galaxies. In particular, we consider the FR II sample by Kozieł-Wierzbowska, & Stasińska (2011), which resulted from cross-identification of the objects included in the Cambridge Catalogues of Radio Sources (3C–9C) with galaxies from the SDSS DR7 main galaxy sample, after excluding quasars and only keeping the objects with clear FR II large-scale radio morphology, investigated manually based on the available radio maps from the NRAO VLA Sky Survey (NVSS) and the Faint Images of the Radio Sky at Twenty-cm (FIRST) survey.

This sample amounts to 401 sources spanning a redshift range from 0.045 up to 0.6, which is well matched to the redshift range in our GPS/CSO sample.

The distribution of the *WISE* colors for the [Koziel-Wierzbowska, & Stasińska \(2011\)](#) sample, in a direct comparison with our sample of GPS/CSOs, is presented in the middle panel of Figure 6. As shown, the analyzed GPS/CSOs, as a population, have significantly different MIR colors than FRIIs. Unlike compact radio galaxies, the evolved FRIIs typically cluster within the area of the color diagram occupied by elliptical galaxies with very little star formation activity. Again, we quantify our statement by running the 2D KS test, and obtain $D = 0.6$ with the corresponding $p = 0.95 \times 10^{-7}$, meaning that the null hypothesis stating that the two samples were drawn from the same distribution, can be safely rejected at the adopted significance level, $\alpha = 0.5$. This result is in fact unexpected, as CSOs (at least the most luminous ones) are widely considered to be a young progenitor of FRII radio galaxies (see, e.g., [Perucho 2016](#), and references therein), and the evolution of radio structures from a compact (< 1 kpc) CSO phase to an evolved (linear sizes ~ 10 s– 100 s kpc) classical double phase, takes only up to ~ 100 Myr, which is much shorter than the timescale required for host galaxy evolution from a late to an early type.

Third, we consider the sample of radio galaxies with confirmed recurrent jet activity, i.e. radio galaxies displaying clearly extended/outer radio lobes (predominantly of the FRII morphological type), in addition to a compact/inner double structure produced during the distinct, newborn jet phase. For these so-called “double-double radio galaxies” (DDRGs; see [Schoenmakers et al. 2000](#)), we use the list recently compiled by [Kuzmicz et al. \(2017\)](#), including 74 sources within a redshift range $0.002 < z < 0.7$. The distribution of the *WISE* colors for this sample is given in the middle panel of Figure 6. The 2D KS test in this case returns $D = 0.31$ with the corresponding $p = 0.065$, meaning that at the significance level of $\alpha = 0.05$, the *WISE* colors for both samples of DDRGs and GPS/CSOs considered here, were drawn from the same distribution.

Finally, we inspect the *WISE* color distribution of our sample of GPS/CSOs against a larger sample of double-lobed radio sources, compiled by [Van Velzen et al. \(2015\)](#) by means of an automated search algorithm applied to the FIRST survey. With the adopted five quality cuts — optimized with respect to the angular size of the respective systems, their radio fluxes, as well as their radio core prominence — the sample of [Van Velzen et al.](#) consists of 24,973 sources that could be safely considered as representing FRII-type radio galaxies, with radio fluxes extending down to the adopted 12 mJy limit. The distribution of the *WISE* colors for this sample is given in the bottom panel of Figure 6. The 2D KS for this and our sample returns a value of $D = 0.45$ with the corresponding $p = 0.11 \times 10^{-3}$, signifying that the two data sets were not drawn from the same distribution. Indeed, it is apparent that one of the main differences here is the lack of GPS/CSOs within the region of the *WISE* color diagram occupied by galaxies forming stars at very high rates (starbursts, luminous- and ultraluminous-infrared galaxies), where, in contrast, many double-lobed FIRST radio sources can be found. This could signify that, ei-

TABLE 2
WISE 2D KS TEST RESULTS

Sample Set	p -value	D value
Asmus et al.	0.048	0.30
Koziel & Stasinska	0.95×10^{-7}	0.60
Kuzmicz et al.	0.065	0.31
Van Velzen et al.	0.11×10^{-3}	0.45

ther the youngest radio sources avoid hosts with very vigorous starformation, or that we are dealing with an observational bias that does not allow for differentiation of compact jets and lobes (and therefore for the “GPS/CSO” classification) in the presence of a strong radio emission from the central starburst region.

The results from all *WISE* color 2D KS tests are summarized in Table 2.

4.2. MIR/X-ray Correlation

A similarity in the MIR colors between our GPS/CSOs and the general population of bright local AGN, prompted us to investigate a correlation between MIR and X-ray luminosities in young radio galaxies. The relationship between MIR and X-ray luminosities in various samples of AGN and in different photon energy ranges have been studied extensively in recent years. Different infrared instruments have been utilized in such analysis, including the low-resolution ISO ([Lutz et al. 2004](#); [Ramos Almeida et al. 2007](#)), *Spitzer* ([Hardcastle et al. 2009](#); [Sazonov et al. 2012](#)), AKARI ([Matsuta et al. 2012](#); [Ichikawa et al. 2012](#)), and *WISE* ([Mateos et al. 2015](#); [Stern 2015](#)) instruments. Studies with high-resolution ground-based telescopes turned out particularly conclusive in this context, as they disclosed a tight correlation between the *nuclear* MIR luminosities and the 2–10 keV luminosities of the targeted AGN, which has important implications for understanding the structure of circumnuclear dusty tori in active galaxies in general (see, e.g., [Horst et al. 2008](#); [Levenson et al. 2009](#); [Gandhi et al. 2009](#); [Asmus et al. 2011, 2015](#)).

In the upper panel of Figure 7 we plot the *IRAS* 12 μ m and the intrinsic (absorption-corrected) 2–10 keV luminosities for the entire sample of our compact radio galaxies (see Table 1; large symbols in the figure), along with the comparison AGN sample by [Asmus et al. \(2014\)](#) introduced in the previous section, for which the 12 μ m luminosities were obtained similarly with the *IRAS* satellite (small grey symbols). In the cases of our sources we utilize the *WISE* 12 μ m measurements; note the $\sim 6.5''$ *WISE* resolution at 12 μ m compared to the *IRAS* angular resolution of $\sim 30''$ at 12 μ m. The differences in angular resolution of the instruments can result in the *WISE* measurements viewing a smaller region of the targeted source. Still, even with such, we are not able to extract solely the innermost nuclear regions of the galaxies, and so all of the sources included in the figure are expected to have a significant contribution from the ISM component in their MIR luminosities, this is in addition to the circumnuclear dust emission (if present). In this context, the solid line in Figure 7 denotes the best-fit linear relation between the logarithms of the luminosities, obtained by [Asmus et al. \(2015\)](#) when using the *high-resolution* MIR observations with ground-based telescopes, for their

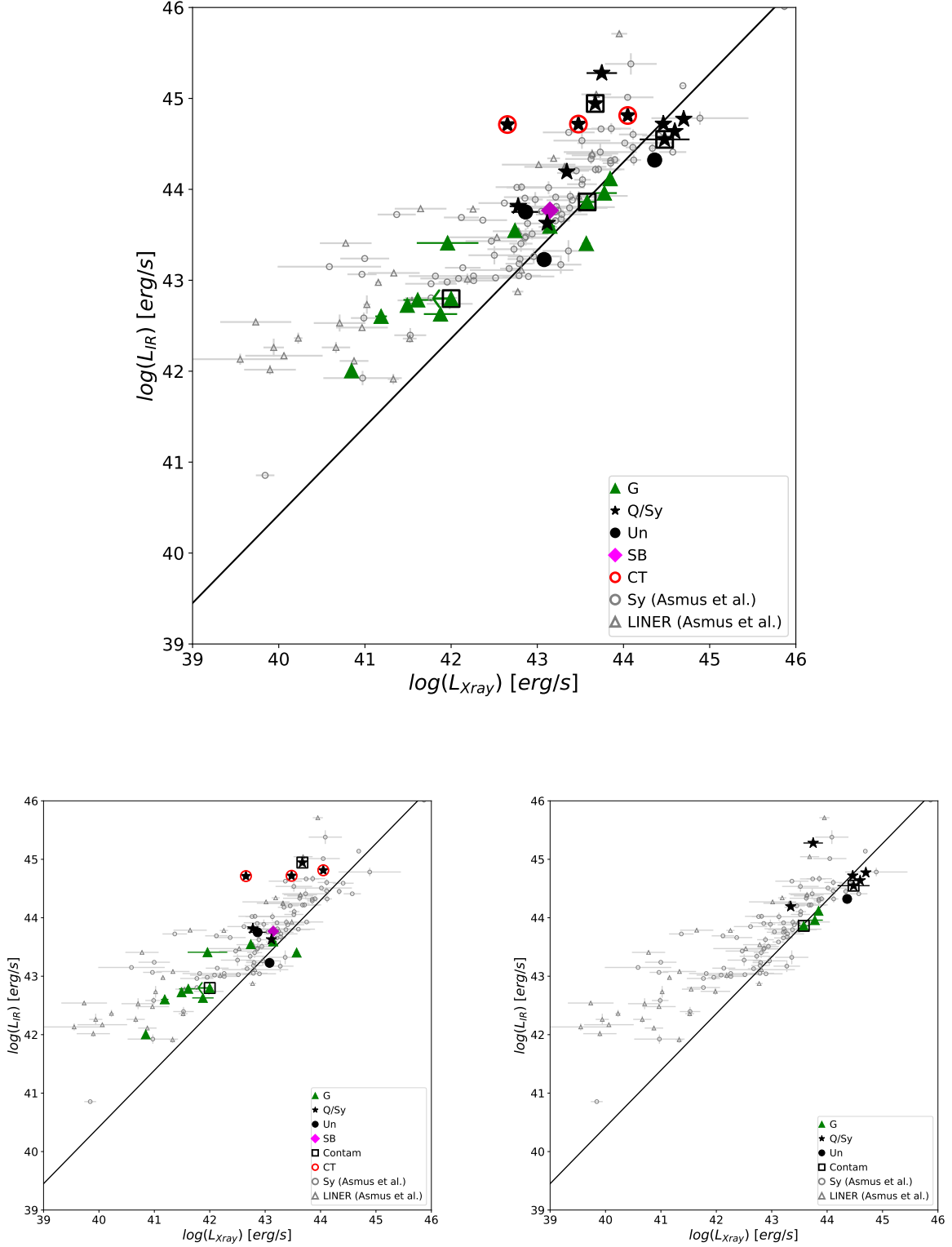


FIG. 7.— Relation of the *WISE* 12 μ m and the intrinsic (absorption-corrected) 2–10 keV luminosities for our compact radio galaxies denoted by large symbols (symbols and colors are the same as in Figure 2). Source 0116 + 319 has an upper limit X-ray luminosity and is marked with a left pointing arrow, visible on the lower left end of the plot. The solid line shows the correlation established for nearby AGN by Asmus et al. (2015) based on the high-angular resolution MIR (ground-based) observations; small grey symbols denote the AGN from the Asmus et al. (2014) sample with *IRAS* 12 μ m luminosities. In the upper panel we show the entire GPS/CSOs sample, in the lower-left panel only the young radio galaxies with $z < 0.4$, and in the lower-right panel only those with $z > 0.4$.

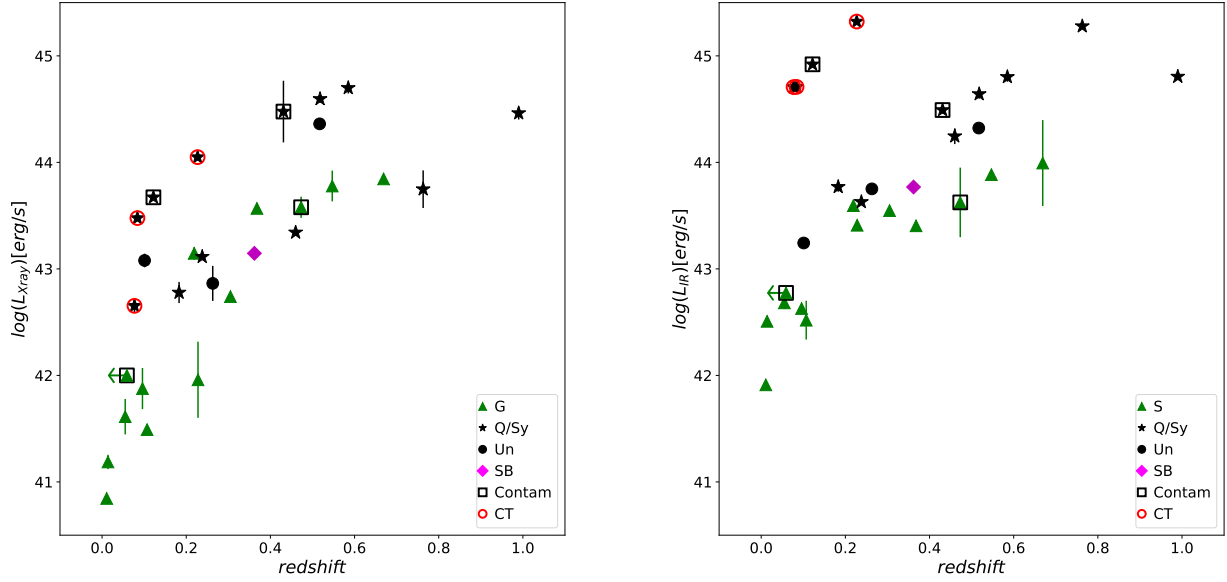


FIG. 8.— The redshift distribution of the intrinsic (absorption-corrected) 2–10 keV luminosities and the *WISE* 12 μ m luminosities of our sample of GPS/CSOs (left and right panels, respectively). Symbols and colors are the same as in Figure 2.

(Asmus et al. 2014) Seyfert+LINER sample,

$$\log\left(\frac{L_{12\mu\text{m}}}{10^{43}\text{ erg s}^{-1}}\right) = 0.33 + 0.97 \log\left(\frac{L_{2-10\text{ keV}}}{10^{43}\text{ erg s}^{-1}}\right). \quad (1)$$

As evident from the figure, the AGN from the comparison sample are located mostly above the best-fit correlation line, as expected keeping in mind the relatively poor angular resolution of *IRAS*, and the fact that the best-fit correlation was established based on sub-arcsec MIR photometry, and so without any significant ISM emission component. Note that the relative contribution of the ISM to the total MIR flux detected with *IRAS* increases for low-luminosity AGN (LINER), as expected.

The distribution of young radio galaxies in the diagram, at the first glance, resembles the distribution of the comparison local AGN sample. The emerging approximate linear scaling between the MIR and X-ray luminosities, along the correlation established by Asmus et al. (2015), could be therefore considered as an indication for the nuclear (disk corona) origin of the observed X-ray fluxes also in the GPS/CSOs sample. Indeed, at least in the case of the confirmed Compton-thick objects, this is the most plausible explanation (Guainazzi et al. 2004; Siemiginowska et al. 2016; Sobolewska et al. 2019a,b). On the other hand, in the framework of the model presented in Stawarz et al. (2008) and Ostorero et al. (2010), where the X-ray radiative output of GPS/CSOs is dominated by the non-thermal emission of the compact radio lobes, one could expect some correlation between the MIR and X-ray luminosities, because in this model X-ray photons are generated predominantly by the inverse-Comptonization of the circumnuclear dust emission by relativistic electrons within compact lobes; we analyze this possibility in more detail in Appendix A below.

On the other hand, an approximately linear

luminosity-luminosity scaling is expected in any flux limited sample of cosmologically distant sources, even in the case of no intrinsic correlations between radiative outputs in various bands (e.g., see the discussion in Singal et al. 2019). Neither our GPS/CSOs sample nor the AGN sample by Asmus et al. (2014) are, strictly speaking, flux-limited (or complete, in that matter). However, the luminosity-redshift distributions of young radio galaxies analyzed here, presented in Figure 8, indicate that we are seriously affected by flux limits in both MIR and X-ray bands, and as a result the observed luminosity-luminosity correlation may be simply due to the fact that higher- z sources have to be more luminous in either band, in order to be included in the sample.

In the lower panels of Figure 7, we plot again the low-resolution *WISE* 12 μ m and the intrinsic (absorption-corrected) 2–10 keV luminosities for our GPS/CSOs, but divided into the redshift bins $z < 0.4$ and $z > 0.4$ (left and right panels, respectively). As shown, the overall scalings are still preserved, although there is a significant difference in the luminosity ratio between the two considered redshift bins. We perform the 2D KS test for the $L_{2-10\text{ keV}} - L_{12\mu\text{m}}$ distributions of our GPS/CSOs and the comparison AGN from Asmus et al. (2014), and obtain $D = 0.26$ with $p = 0.1$ for the entire sample of young radio galaxies, $D = 0.26$ with $p = 0.25$ when only young radio galaxies at redshifts $z < 0.4$ are considered, and $D = 0.7$ with $p = 1.8 \times 10^{-4}$ for the GPS/CSOs with $z > 0.4$ (see Table 3). These values imply that our null hypothesis — stating that, in the “low-resolution MIR luminosity vs. absorption-corrected X-ray luminosity” representation, the GPS/CSOs and the comparison AGN samples are drawn from the same distribution — can be rejected only for high-redshift sources.

Those high-redshift targets, on the other hand, appear (visually) to match very well the best-fit correla-

TABLE 3
IR–XRAY 2D KS TEST RESULTS

Sample Set	p -value	D value
Full Sample	0.10	0.26
$z < 0.4$	0.25	0.26
$z > 0.4$	1.8×10^{-4}	0.7

tion line of Asmus et al. (2015) established based on sub-arcsec MIR photometry of local AGN. This should not be surprising, however, noting that at high MIR luminosities characterizing our $z > 0.4$ sources, $L_{12\mu\text{m}} \geq 3 \times 10^{43} \text{ erg s}^{-1}$, any contribution from the ISM component with a moderate star formation rate (up to $\sim 10 M_{\odot} \text{ yr}^{-1}$), is expected to be rather minor, and so the fluxes extracted even with low-resolution instruments such as *IRAS* or *WISE*, should be dominated by the radiative output of circumnuclear dust.

On the related note, we comment that in the case of $z < 0.4$ young radio galaxies, the only ones with $L_{12\mu\text{m}}$ exceeding $10^{44} \text{ erg s}^{-1}$, are the three Compton-thick objects 1404+286, 1511+0518 and 2021+614, and the peculiar 1345+125, which can also be classified as Ultraluminous Infrared Galaxies (see Rodríguez Zaurín et al. 2009). Those four sources appear in fact over-luminous in MIR for their given intrinsic (absorption-corrected) X-ray luminosities when compared to the general local AGN population, as well as other local GPS/CSOs (see in this context the right panel in Figure 8).

4.3. Gamma-ray Emitters 1718–649 & 1146+596

1718–649 and 1146+596 are the two lowest-luminosity sources in our sample, which are rather unique objects for several reasons. 1718–649 is particularly young and compact ($LS \simeq 2 \text{ pc}$, $\tau \simeq 100 \text{ yr}$; Giroletti & Polatidis 2009), located at the distance of 60 Mpc only, and most importantly, it is the first bona-fide CSO detected in the high-energy γ -ray range with *Fermi* Large Area Telescope (LAT; see the analysis and the discussion in Migliori et al. 2016). 1146+596 is characterized by a much larger $LS \simeq 933 \text{ pc}$ (Taylor et al. 1998; Perlman et al. 2001), but located at a comparable distance of 47 Mpc, and recently associated with the γ -ray source 4FGL J1149.0+5924 in the *Fermi* LAT 8-Year Point Source Catalog (4FGL; The *Fermi*-LAT collaboration 2019). The question follows if the observed γ -ray emission in both sources is related to the jet activity and compact radio lobes in particular (Stawarz et al. 2008; Kino et al. 2009), or is instead due to the star formation activity within the hosts, analogous to the LAT-detected, star-forming and starburst galaxies (Ackermann et al. 2012; Hayashida et al. 2013; Rojas-Bravo & Araya 2016).

In order to address this question, we have collected all archival infrared data for both sources, including near-infrared 2MASS and MIR *Spitzer* spectra, as well as mm fluxes from WMAP, and estimated the integrated 8 – 1000 μm luminosities, and next the star-formation rates assuming the Kennicutt (1998) scaling relation

$$\frac{\text{SFR}}{M_{\odot} \text{ yr}^{-1}} = 1.7 \epsilon \times \frac{L_{8-1000 \mu\text{m}}}{10^{10} L_{\odot}}, \quad (2)$$

with the initial mass function factor $\epsilon = 0.79$ (Acker-

mann et al. 2012). The resulting values, given in Table 4, are consistent with the SFR estimates by Willett et al. (2010) for 1718–649, based on either Ne lines or PAH features in the *Spitzer* high-resolution spectra (see the Table). In the case of 1146+596 we achieve a lower SFR estimate based on the integrated luminosity, which may be due in part to poor data quality (i.e. lack of data points over the infrared range) as well as due to the fact that some MIR emission can come from the dust heated by old stellar populations and not indeed by star formation itself. As both sources are the weakest MIR emitters in the sample, the SFR at the corresponding level of $\sim 1 M_{\odot} \text{ yr}^{-1}$ should be considered as the limiting value for young radio galaxies analyzed here. Assuming further the best-fit correlation derived by Ackermann et al. (2012) for the LAT-detected, star-forming and starburst galaxies,

$$\log \left(\frac{L_{0.1-100 \text{ GeV}}^{\text{ISM}}}{10^{39} \text{ erg s}^{-1}} \right) = 1.17 \log \left(\frac{L_{8-1000 \mu\text{m}}}{10^{10} L_{\odot}} \right) + 0.28, \quad (3)$$

we next derived the ISM-related 0.1 – 100 GeV luminosities for the two targets, which are both at the level of $\sim 10^{38-39} \text{ erg s}^{-1}$, as listed in Table 4.

Meanwhile, the integrated 0.1 – 100 GeV photon flux of the high-energy γ -ray counterpart of 1718–649 provided by Migliori et al. (2016), $(11.5 \pm 0.3) \times 10^{-9} \text{ ph cm}^{-2} \text{ s}^{-1}$, along with the best-fit photon index $\Gamma_{\gamma} = 2.9 \pm 0.3$, yields the luminosity $L_{0.1-100 \text{ GeV}} \sim 2 \times 10^{42} \text{ erg s}^{-1}$, which is three orders of magnitude larger than the one expected for the ISM emission as estimated above. Similarly, for 1146+596, based on the integrated 1 – 100 GeV photon flux of the high-energy γ -ray counterpart provided in 4FGL, $(2.17 \pm 0.35) \times 10^{-10} \text{ ph cm}^{-2} \text{ s}^{-1}$, along with the best-fit photon index $\Gamma_{\gamma} = 2.06 \pm 0.11$, we derive the luminosity $L_{0.1-100 \text{ GeV}} \sim 6 \times 10^{41} \text{ erg s}^{-1}$, which is again orders of magnitude larger than the expected emission for the ISM component alone.

Hence, we conclude that the γ -ray emission detected with *Fermi*-LAT from 1718–649 and 1146+596, is undoubtedly related to the jet activity in the sources, and not the star formation activity. This strengthens the expectation that compact lobes/jets in young radio galaxies are in general γ -ray emitters. Moreover, we note that the two CSOs detected by *Fermi* LAT so far, are in fact the *nearest* objects in our sample. This suggests that with a longer accumulation of the LAT data, the most promising candidates for the γ -ray detection should be 0116+319 and 0402+379 (luminosity distances $\sim 250 \text{ Mpc}$; see Table 1), and — even more excitingly — the two Compton-thick CSOs 1404+286 and 1511+0518 (luminosity distances $\sim 350 \text{ Mpc}$).

5. CONCLUSIONS

In this paper we have discussed the MIR properties of the most compact (GPS/CSO-type) radio galaxies, based predominantly on the lower-resolution MIR data provided by *WISE* and *IRAS* satellites (augmented in a few cases by the *Spitzer* observations). We have restricted our analysis to only those objects which have been observed in X-rays with either XMM-*Newton* or *Chandra*, and this resulted in the sample of 29 objects.

The inspection of optical images for the targets, implies

TABLE 4
SFRs, IR LUMINOSITIES, AND γ -RAY LUMINOSITIES OF 1718–649 & 1146+596

Name	$L_{8-1000\mu\text{m}}$ erg s^{-1}	SFR_{IR} $M_{\odot} \text{ yr}^{-1}$	SFR_{Ne} $M_{\odot} \text{ yr}^{-1}$	SFR_{PAH} $M_{\odot} \text{ yr}^{-1}$	$L_{0.1-100 \text{ GeV}}^{[\text{ISM}]}$ erg s^{-1}	$L_{0.1-100 \text{ GeV}}$ erg s^{-1}
(1)	(2)	(3)	(4)	(5)	(6)	(7)
1146+596	5.5×10^{42}	~ 0.13	0.5 ± 0.1	~ 0.3	$\sim 2 \times 10^{38}$	$\sim 0.6 \times 10^{42}$
1718–649	3.7×10^{43}	~ 0.89	1.8 ± 0.1	~ 0.8	$\sim 2 \times 10^{39}$	$\sim 2 \times 10^{42}$

col(1) — Name of the source; **col(2)** — Integrated infrared luminosity derived from archival 8 – 1000 μm data; **col(3)** — Star formation rate for the given integrated infrared luminosity in col(2); **col(4)** — Star formation rate calculated from Ne emission lines in Willett et al. (2010); **col(5)** — Star formation rate calculated from Polycyclic aromatic hydrocarbon (PAH) emission lines in Willett et al. (2010); **col(6)** — 0.1 – 100 GeV luminosity estimated emission based on the integrated infrared flux in col(2); **col(7)** — The observed *Fermi*-LAT 0.1 – 100 GeV luminosity.

that the analyzed GPS/CSOs are hosted predominantly by red/yellow galaxies with an elliptical shape, with several cases containing distorted morphology or signs of galaxy interaction.

In our sample we found a variety of *WISE* colors, suggesting that the MIR continua of the studied sources are contributed not exclusively by the circumnuclear dust, but also by the ISM of host galaxies, and in a few cases even by the non-thermal emission of compact jets and lobes. Such a diversity resembles a general population of bright local AGN (Asmus et al. 2014). In particular, we found that young radio galaxies with the MIR emission dominated by the ISM component, populate almost uniformly the entire region occupied by galaxies (from elliptical to starbursts) with a wide range of a pronounced star formation activity (rates $\geq 0.5 M_{\odot} \text{ yr}^{-1}$). This constitutes a significant difference with the population of the evolved ordinary FR II radio galaxies (Kozieł-Wierzbowska, & Stasińska 2011), which are clustered within the area of the MIR color diagram occupied by elliptical galaxies with very little star formation activity. This unexpected result — keeping in mind the general expectation that luminous CSOs are young progenitor of FR II radio galaxies — could signal a negative feedback at work, meaning that that expanding jets and lobes, during their evolution from a compact CSO phase up to the evolved classical double phase, suppress the star formation in galactic hosts. Yet we also found that the distribution of the MIR colors in our GPS/CSOs sample is statistically indistinguishable from the distribution of MIR colors of large-scale radio galaxies but with recurrent jet activity (DDRGs; Kuźmierz et al. 2017). We quantified our statement by performing two-dimensional Kolmogorov-Smirnov tests.

All these findings seems therefore to imply that (1) triggering radio jets in AGN does not differentiate between elliptical hosts with substantially different fractions of young stars, and (2) it is the jet duty cycle — and not the jet launching itself — which is related to the star formation rate within the host, in that radio galaxies hosted by galaxies with more pronounced population of young stars are either typically short lived (i.e., not surviving long enough to form an extended FR II structure), or characterized by a highly modulated/recurrent jet activity. We note in this context that, in the accompanying paper Wójtowicz et al. (2019), we derived the bolometric luminosities of the accretion disks and the black hole masses for about half of the GPS/CSOs sample analyzed

here, and demonstrated that the corresponding accretion rates are in all the cases high, namely between 1% and 20% in Eddington units.

The caveat here is the *WISE* color distribution of our sample of GPS/CSOs against a larger sample of double-lobed radio sources from Van Velzen et al. (2015), suggest at the same time that the youngest radio sources avoid hosts with very vigorous starformation. However, a more plausible explanations is that there exists an observational bias which does not allow for differentiation of compact jets and lobes (and therefore for the “GPS/CSO” classification) in the presence of a strong radio emission from the central starburst region.

The distribution of the sub-sample of our sources with $z < 0.4$ on the low-resolution MIR vs. absorption-corrected X-ray luminosity plane is consistent with the distribution of a sample of local AGN on the same plane (Asmus et al. 2014). High-resolution (sub-arcsec) MIR photometry of the studied sources, along with deep X-ray exposures, are required in order to make any conclusive statements on the origin of the emerging luminosity-luminosity correlation.

Interestingly, all the confirmed Compton-thick objects in the sample — 1404+286, 1511+0518 and 2021+614 — are characterized by the *WISE* colors consistent with quasar identification, and, in addition, appear over-luminous in MIR for the given level of their intrinsic X-ray emission when compared to the general local AGN population as well as other local GPS/CSOs. Hence, *WISE* color diagnostics and photometry could, in general, be considered as a very useful tool when selecting candidates for Compton-thick AGN among compact radio galaxies. Note in this context that, compact radio sources are particularly abundant in flux-limited radio samples, constituting $\sim 10\%$ of the bright radio-source population (O’Dea 1998; Sadler 2016).

Finally, we discussed in more detail the particular case of the γ -ray-detected 1718–649 and 1146+596. By means of a comparison with the sample of star-forming and starburst galaxies detected with *Fermi*-LAT, we have argued that the γ -ray flux observed from these, is undoubtedly related to the jet activity in the sources, and not due to the star formation activity. This strengthens the expectation that compact lobes/jets in young radio galaxies are in general γ -ray emitters, albeit relatively weak so that the *Fermi*-LAT detections are currently limited to the two the nearest objects in the sample.

This work was supported by the Fulbright Program and in collaboration with the Astronomical Observatory of the Jagiellonian University. EK, LS, AW, and VM were supported by Polish NSC grant 2016/22/E/ST9/00061. L.O. acknowledges partial support from the INFN Grant InDark and the grant of the Italian Ministry of Education, University and Research (MIUR) (L.232/2016) ECCELLENZA1822 D206 - Dipartimento di Eccellenza 2018-2022 Fisica awarded to the Dept. of Physics of the University of Torino. M.S. and A.S. were supported by NASA contract NAS8-03060 (Chandra X-ray Center). Work at the Naval Research Laboratory is supported by the Chief of Naval Research.

The authors thank D. Asmus, P. Gandhi, and A. Kuźmierz for the discussion and comments.

This publication makes use of data products from the Wide-field Infrared Survey Explorer, which is a joint project of the University of California, Los Angeles, and the Jet Propulsion Laboratory/California Institute of Technology, funded by the National Aeronautics and Space Administration.

This research has made use of the NASA/IPAC Infrared Science Archive, which is operated by the Jet Propulsion Laboratory, California Institute of Technology, under contract with the National Aeronautics and Space Administration.

Funding for the Sloan Digital Sky Survey IV has been provided by the Alfred P. Sloan Foundation, the U.S. Department of Energy Office of Science, and the Participating Institutions. SDSS acknowledges support and resources from the Center for High-Performance Computing at the University of Utah. The SDSS web site is www.sdss.org.

The Pan-STARRS1 Surveys (PS1) and the PS1 public science archive have been made possible through contributions by the Institute for Astronomy, the University of Hawaii, the Pan-STARRS Project Office, the Max-Planck Society and its participating institutes, the Max Planck Institute for Astronomy, Heidelberg and the Max Planck Institute for Extraterrestrial Physics, Garching, The Johns Hopkins University, Durham University, the University of Edinburgh, the Queen's University Belfast, the Harvard-Smithsonian Center for Astrophysics, the Las Cumbres Observatory Global Telescope Network Incorporated, the National Central University of Taiwan, the Space Telescope Science Institute, the National Aeronautics and Space Administration under Grant No. NNX08AR22G issued through the Planetary Science Division of the NASA Science Mission Directorate, the National Science Foundation Grant No. AST-1238877, the University of Maryland, Eotvos Lorand University (ELTE), the Los Alamos National Laboratory, and the Gordon and Betty Moore Foundation.

REFERENCES

- Abolfathi, B., Aguado, D. S., Aguilar, G., et al. 2018, *ApJS*, 235, 42
- Ackermann, M., Ajello, M., Allafort, A., et al. 2012, *ApJ*, 755, 164
- Allison, J. R., Mahony, E. K., Moss, V. A., et al. 2019, *MNRAS*, 482, 2934
- Asmus, D., Gandhi, P., Smette, A., Hönig, S. F., & Duschl, W. J. 2011, *A&A*, 536, A36
- Asmus, D., Hönig, S. F., Gandhi, P., Smette, A., & Duschl, W. J. 2014, *MNRAS*, 439, 1648
- Asmus, D., Gandhi, P., Hönig, S. F., Smette, A., & Duschl, W. J. 2015, *MNRAS*, 454, 766
- Beuchert, T., Rodríguez-Ardila, A., Moss, V. A., et al. 2018, *A&A*, 612, L4
- Chambers, K. C., Magnier, E. A., Metcalfe, N., et al. 2016, *arXiv e-prints*, arXiv:1612.05560
- Czerny, B., & You, B. 2016, *Astronomische Nachrichten*, 337, 73
- de Vries, W. H., Barthel, P. D., & O'Dea, C. P. 1997, *A&A*, 321, 105
- Dicken, D., Tadhunter, C., Axon, D., et al. 2012, *ApJ*, 745, 172
- Fanti, C., Pozzi, F., Fanti, R., et al. 2000, *A&A*, 358, 499
- Fasano, G., & Franceschini, A. 1987, *MNRAS*, 225, 155
- The Fermi-LAT collaboration 2019, *arXiv e-prints*, arXiv:1902.10045
- Gandhi, P., Horst, H., Smette, A., et al. 2009, *A&A*, 502, 457
- Giroletti, M., & Polatidis, A. 2009, *Astronomische Nachrichten*, 330, 193
- Głowacki, M., Allison, J. R., Sadler, E. M., et al. 2017, *MNRAS*, 467, 2766
- Guainazzi, M., Siemiginowska, A., Rodríguez-Pascual, P., & Stanghellini, C. 2004, *A&A*, 421, 461
- Guainazzi, M., Siemiginowska, A., Stanghellini, C., et al. 2006, *A&A*, 446, 87
- Hardcastle, M. J., Evans, D. A., & Croston, J. H. 2009, *MNRAS*, 396, 1929
- Hayashida, M., Stawarz, L., Cheung, C. C., et al. 2013, *ApJ*, 779, 131
- Heckman, T. M., O'Dea, C. P., Baum, S. A., & Laurikainen, E. 1994, *ApJ*, 428, 65
- Horst, H., Gandhi, P., Smette, A., & Duschl, W. J. 2008, *A&A*, 479, 389
- Ichikawa, K., Ueda, Y., Terashima, Y., et al. 2012, *ApJ*, 754, 45
- Jia, J., Ptak, A., Heckman, T., & Zakamska, N. L. 2013, *ApJ*, 777, 27
- Kawakatu, N., Nagai, H., & Kino, M. 2008, *ApJ*, 687, 141
- Kellermann, K. I., Lister, M. L., Homan, D. C., et al. 2004, *ApJ*, 609, 539
- Kennicutt, R. C., Jr. 1998, *ApJ*, 498, 541
- Kino, M., Ito, H., Kawakatu, N., & Nagai, H. 2009, *MNRAS*, 395, L43
- Kozieł-Wierzbowska, D., & Stasińska, G. 2011, *MNRAS*, 415, 1013
- Kunert-Bajraszewska, M., Labiano, A., Siemiginowska, A., & Guainazzi, M. 2014, *MNRAS*, 437, 3063
- Kuźmierz, A., Jamroz, M., Kozieł-Wierzbowska, D., et al. 2017, *MNRAS*, 471, 3806
- Levenson, N. A., Radomski, J. T., Packham, C., et al. 2009, *ApJ*, 703, 390
- Lutz, D., Maiolino, R., Spoon, H. W. W., & Moorwood, A. F. M. 2004, *A&A*, 418, 465
- Massaro, F., D'Abrusco, R., Tosti, G., et al. 2012, *ApJ*, 750, 138
- Mateos, S., Alonso-Herrero, A., Carrera, F. J., et al. 2012, *MNRAS*, 426, 3271
- Mateos, S., Carrera, F. J., Alonso-Herrero, A., et al. 2015, *MNRAS*, 449, 1422
- Matsuta, K., Gandhi, P., Dotani, T., et al. 2012, *ApJ*, 753, 104
- Migliori, G., Siemiginowska, A., Kelly, B. C., et al. 2014, *ApJ*, 780, 165
- Migliori, G., Siemiginowska, A., Sobolewska, M., et al. 2016, *ApJ*, 821, L31
- O'Dea, C. P. 1998, *PASP*, 110, 493
- O'Dea, C. P. 2016, *Astronomische Nachrichten*, 337, 141
- Ostorero, L., Moderski, R., Stawarz, L., et al. 2010, *ApJ*, 715, 1071
- Ostorero, L., Morganti, R., Diaferio, A., et al. 2017, *ApJ*, 849, 34
- Peacock, J. A. 1983, *MNRAS*, 202, 615
- Perlman, E. S., Stocke, J. T., Conway, J., & Reynolds, C. 2001, *AJ*, 122, 536
- Perucho, M. 2016, *Astronomische Nachrichten*, 337, 18
- Ramos Almeida, C., Pérez García, A. M., Acosta-Pulido, J. A., & Rodríguez Espinosa, J. M. 2007, *AJ*, 134, 2006
- Rodríguez Zaurín, J., Tadhunter, C. N., & González Delgado, R. M. 2009, *MNRAS*, 400, 1139
- Rojas-Bravo, C., & Araya, M. 2016, *MNRAS*, 463, 1068
- Romani, R. W., Forman, W. R., Jones, C., et al. 2014, *ApJ*, 780, 149
- Sadler, E. M. 2016, *Astronomische Nachrichten*, 337, 105
- Sazonov, S., Willner, S. P., Goulding, A. D., et al. 2012, *ApJ*, 757, 181
- Schoenmakers, A. P., de Bruyn, A. G., Röttgering, H. J. A., et al. 2000, *MNRAS*, 315, 371
- Siemiginowska, A., LaMassa, S., Aldcroft, T. L., Bechtold, J., & Elvis, M. 2008, *ApJ*, 684, 811
- Siemiginowska, A. 2009, *Astronomische Nachrichten*, 330, 264

Siemiginowska, A., Sobolewska, M., Migliori, G., et al. 2016, *ApJ*, 823, 57
Singal, J., Petrosian, V., Haider, J., et al. 2019, *ApJ*, 877, 63
Sobolewska, M., Siemiginowska, A., Guainazzi, M., et al. 2019a, *ApJ*, 871, 71
Sobolewska, M., Siemiginowska, A., Guainazzi, M., et al. 2019b, *ApJ*, 884, 166
Stawarz, L., Ostorero, L., Begelman, M. C., et al. 2008, *ApJ*, 680, 911
Stern, D. 2015, *ApJ*, 807, 129
Stern, D., Assef, R. J., Benford, D. J., et al. 2012, *ApJ*, 753, 30
Tadhunter, C. 2016, *Astronomische Nachrichten*, 337, 159
Tadhunter, C., Holt, J., González Delgado, R., et al. 2011, *MNRAS*, 412, 960
Taylor, G. B., Wrobel, J. M., & Vermeulen, R. C. 1998, *ApJ*, 498, 619
Tengstrand, O., Guainazzi, M., Siemiginowska, A., et al. 2009, *A&A*, 501, 89
Torresi, E., Grandi, P., Capetti, A., Baldi, R. D., & Giovannini, G. 2018, *MNRAS*, 476, 5535

Ueda, Y., Ishisaki, Y., Takahashi, T., Makishima, K., & Ohashi, T. 2005, *ApJS*, 161, 185
van Velzen S., Falcke H., Körding E. 2015, *MNRAS*, 446, 2985
Vink, J., Snellen, I., Mack, K.-H., & Schilizzi, R. 2006, *MNRAS*, 367, 928
Wagner, A. Y., Bicknell, G. V., Umemura, M., Sutherland, R. S., & Silk, J. 2016, *Astronomische Nachrichten*, 337, 167
Watson, M. G., Schröder, A. C., Fyfe, D., et al. 2009, *A&A*, 493, 339
Willett, K. W., Stocke, J. T., Darling, J., & Perlman, E. S. 2010, *ApJ*, 713, 1393
Wójtowicz, A., Stawarz, L., Cheung, C. C., et al. 2019, *arXiv e-prints*, arXiv:1911.01197
Wright, E. L., Eisenhardt, P. R. M., Mainzer, A. K., et al. 2010, *AJ*, 140, 1868

APPENDIX

NON-THERMAL X-RAY EMISSION OF YOUNG RADIO GALAXIES

Below we provide a very simplified approximation for the expected X-ray luminosity of compact radio lobes in compact radio galaxies, following [Stawarz et al. \(2008\)](#). In this model, the monochromatic lobes' luminosity is

$$\varepsilon L_\varepsilon \simeq \frac{2}{3} c \sigma_T V U_{\text{MIR}} [\gamma^3 N_e(\gamma)]_{\gamma=\sqrt{\varepsilon/\varepsilon_0}}, \quad (\text{A1})$$

where V is the volume of the lobes, U_{MIR} is the energy density of the circumnuclear dust emission at the position of the lobes, $N_e(\gamma)$ is the energy spectrum of ultrarelativistic electrons with Lorentz factors γ , and ε_0 is the energy of the Compton-upscattered seed photon. By following the evolution of the electrons subjected to radiative and adiabatic energy losses within the expanding lobes, [Stawarz et al. \(2008, section 3.1. therein\)](#) showed that in the case of a single power-law injection rate $Q_e(\gamma) = k \gamma^{-s}$ with $s \geq 2.0$ and the normalization constant k , for a given age of a source τ the electron spectrum can be approximated by $N_e(\gamma) \simeq \tau (k/V) \times f(\gamma)$, where $f(\gamma) = \gamma^{-s}$ for $\gamma < \gamma_{\text{cr}}$ and $f(\gamma) = \gamma_{\text{cr}} \gamma^{-s-1}$ otherwise, and $\gamma_{\text{cr}} \propto L_j^{-1/2}$ is the cooling break energy depending on the jet's total kinetic luminosity L_j . We further assume an energy equipartition between ultrarelativistic electrons and the lobes' magnetic field, meaning $V U_e \simeq \tau L_j$, where $U_e \equiv \int \gamma m_e c^2 N_e(\gamma) d\gamma$ is the electron energy density. Note that $\tau = \text{LS}/v_h$, where LS is the linear size of the lobes, taken as the distance between the the jet termination shocks (hereafter “hotspots”) in a given source, and v_h is the expansion velocity of the lobes, measured as the separation velocity between the hotspots.

For the seed photon's energy density at the position of the lobes, we simply take $U_{\text{MIR}} \simeq L_{\text{MIR}}/4\pi R^2 c$, where $R \simeq (\sqrt[3]{3}/8) \text{LS}$ is the effective radius of the lobes, approximated as an ellipsoid with a semi-major axis $a = \text{LS}/2$ and semi-minor axis $b = a/4$ (see in this context [Kawakatu et al. 2008](#); [Wójtowicz et al. 2019](#)), and $L_{\text{MIR}} \sim 3 \times L_{12 \mu\text{m}}$ is the total MIR luminosity of the hot dusty torus, with a mean photon energy $\varepsilon_0 = hc/\lambda_0$ for $\lambda_0 \sim 12 \mu\text{m}$. Given all the above, one may find

$$\frac{L_{2-10 \text{ keV}}}{L_{12 \mu\text{m}}} \simeq \frac{32 \sigma_T}{3^{2/3} \pi m_e c^2} \frac{L_j}{v_h \text{LS}} \frac{\int_2^{10} [\gamma^3 f(\gamma)]_{\gamma=\sqrt{\frac{x}{x_0}}} \frac{dx}{x}}{\int_1^{1e5} \gamma f(\gamma) d\gamma}, \quad (\text{A2})$$

where $x \equiv \varepsilon/\text{keV}$. We next note, for the injection index $s = 2.5$ corresponding to the mean radio spectral index of compact radio galaxies ([de Vries et al. 1997](#)), the last term in the above relation containing integrals over $f(\gamma)$, depends only weakly on the jet kinetic power, and within a wide range of L_j reads as ~ 20 . Hence, a very simple approximate scaling emerges

$$\frac{L_{2-10 \text{ keV}}}{L_{12 \mu\text{m}}} \sim \left(\frac{L_j}{10^{45} \text{ erg s}^{-1}} \right) \left(\frac{\text{LS}}{\text{pc}} \right)^{-1} \left(\frac{v_h}{c} \right)^{-1}. \quad (\text{A3})$$

One should keep in mind that the scaling relation derived above relies on several crude approximations, in particular the spectral shape of the electron injection function, so it is possible that in several cases a more detailed modelling, taking into account the exact shape of the radio continua of the studied sources (as presented in [Ostorero et al. 2010](#)), could result in an elevated level of the expected inverse-Compton emission of compact lobes in the X-ray domain. Additionally, the true jet kinetic luminosities may be larger than the minimum values utilized here. Keeping all these caveats in mind, we conclude that a significant contribution of the non-thermal emission of compact lobes to the observed radiative output of compact radio galaxies in the X-ray domain, remains a plausible option, and that the resulting X-ray luminosity should scale with the MIR luminosity of dusty tori, albeit with a wider scatter due to the dependance of the $L_{2-10 \text{ keV}}/L_{12 \mu\text{m}}$ ratio on the jet kinetic luminosity L_j , the linear size of radio lobes, and the expansion velocity of compact lobes v_h .